Tracking dynamic threat imminence

Christian Meyer[1,*], Srikanth Padmala[1,2,*] & Luiz Pessoa[1,2,3]

[1]Department of Psychology, University of Maryland, College Park, MD, USA

[2]Neuroscience and Cognitive Sciences program, University of Maryland, College Park, MD, USA

[3]Maryland Neuroimaging Center, University of Maryland, College Park, MD, USA

*Authors contributed equally to this work

Running head: Dynamic aversive anticipation

Number of Pages: 37

Number of Figures & Tables: 11 Figures and 10 Tables

Number of Words: Abstract (238), Introduction (650), Discussion (1496)

Corresponding author:

Luiz Pessoa
Department of Psychology
1147 Biology-Psychology Building
University of Maryland, College Park, MD 20742
Email: pessoa@umd.edu

Conflict of Interest: The authors declare no competing financial interests.

Acknowledgements
The authors acknowledge funding from the National Institute of Mental Health (R01 MH071589) and a National Science Foundation Graduate Research Fellowship to Srikanth Padmala. We would like to thank Brenton McMenamin for paradigm development, Dan Levitas for data collection, Jason Smith for help with processing scripts, Mahshid Najafi for help with initial pre-processing of the fMRI data, and Nicole Friedman and Jessica Berman for help with subject recruitment. The authors also acknowledge the Behavioral and Social Sciences College, University of Maryland, high performance computing resources (http://bsos.umd.edu/oacs/bsos-high-performance) made available for conducting the research reported in this paper.

Abstract

During many real-life situations, multiple factors interact to determine threat level. Importantly, their interaction evolves over time, such that aversive anticipation changes dynamically. Studies have taken initial strides at understanding how factors such as proximity and direction influence responses to threat. However, by and large, these studies have investigated the contributions of independent threat-related factors. Therefore, little is known about how they *dynamically interact* during aversive anticipation. To address these gaps, in the current functional MRI study involving healthy adult human volunteers, we investigated interactions between proximity, direction, and speed during a dynamic threat-of-shock paradigm. Whereas some brain regions tracked individual threat-related factors, others were also sensitive to combinations of these variables, including their three-way combination. For example, the hippocampus was particularly sensitive to threat proximity. In contrast, among others, signals in the anterior insula and PAG tracked the interaction of all three factors. In the right amygdala, we observed a proximity by direction interaction, but in the opposite direction as the anterior insula and PAG; retreat vs. approach responses were stronger when threat was closer compared to farther. Thus, in the context of our task, intriguingly, it appears that the amygdala provided a safety-related response, especially when threat was closer. Taken together, our study refines our understanding of the brain mechanisms involved during aversive anticipation in human brain. Importantly, it emphasizes that threat processing should be understood in a manner that is both context sensitive and dynamic.

Significance Statement

In a human functional MRI study, we investigated how multiple threat-related factors (proximity, direction, and speed) interact when varied continuously. In particular, we asked whether signal fluctuations in brain regions track threat-related factors dynamically? If so, to what factor(s) and factor combinations are they sensitive? Whereas some brain regions reacted to individual threat-related factors, several regions were sensitive to particular combinations of factors (for instance, threat proximity and whether threat approached or retreated). Overall, our study refines our understanding of the mechanisms involved during aversive anticipation in the human brain. Importantly, it emphasizes that threat processing should be understood in a manner that is both context sensitive and dynamic.

Introduction

Anticipation of aversive events leads to a repertoire of changes in behavioral, physiological, and brain responses that contribute to adequate handling of the negative consequences of such events. At the same time, abnormalities in aversive anticipatory processing are thought to underlie many mental disorders, such as anxiety and depression (Grupe and Nitschke, 2013; Dillon et al., 2014). Hence, understanding the brain mechanisms of aversive anticipation is important from both basic and clinical standpoints.

In humans, aversive anticipation has been investigated by employing paradigms in which punctate cues signal an upcoming negative event (Jensen et al., 2003; Simmons et al., 2006; Grupe et al., 2013) , or by blocked manipulations with constant threat level (McMenamin et al., 2014; Vytal et al., 2014). However, during most real-world situations, aversive anticipation changes dynamically over time. An important factor in determining threat level is proximity, as when a prey reacts differently to the presence of a predator when the latter is proximal compared to distant (Figure 1A). For example, when a rat is far from a cat, it will freeze or flee if an escape route is available; when the rat is placed nearer to the cat, it will display active fight or flight (Blanchard and Blanchard, 1990; Blanchard et al., 2011). Another factor involves direction/speed, such as whether the threat is approaching vs. retreating, and how fast (Fanselow, 1988; Figure 1B). Some studies have taken initial strides at investigating how these factors influence processing during aversive anticipation. For instance, the contrast of proximal vs. distal threats revealed functional MRI (fMRI) responses in a host of brain regions, including the anterior insula, midbrain periaqueductal gray (PAG), and bed nucleus of the stria terminalis (BNST) (Mobbs et al., 2010; Somerville et al., 2010); evidence for amygdala involvement linked to threat proximity is mixed (Mobbs et al., 2010; Somerville et al., 2010). Similarly, comparison of approaching vs. retreating threats has revealed responses in the anterior insula, BNST, and amygdala (Mobbs et al., 2010).

Thus far, studies have considered the effects of threat proximity and direction/speed independently. Hence, it is currently unknown how such factors potentially interact in the brain during aversive anticipation (Figure 1C). However, this is major gap in our knowledge base because empirical findings have extensively documented interactions between threat-related factors, which have produced several influential theoretical accounts (for excellent discussion, see Mobbs et al., 2015). Although some conceptualizations have focused on major stages of threat processing, such as the "pre-encounter phase" (when the risk of threat exists without detectable presence of danger), Fanselow and Lester (1988) describe a "threat imminence continuum", and Kavaliers and Choleris (2001) propose an "apprehension gradient" that ranges from no interest to complete preoccupation with the predator. In all, it is not only important to investigate how multiple threat-related factors interact but to understand how the brain tracks them continuously. In particular, do signal fluctuations in brain regions track threat-related factors dynamically? If so, to what factor(s) and factor combinations are they sensitive?

To address these questions, we devised a paradigm in which threat was dynamically modulated during fMRI scanning. Two circles moved on the screen, sometimes moving closer and sometimes moving apart, and at varying speeds (Figure 2). Participants were instructed to pay attention to the circles on the screen; if the circles touched, an unpleasant shock was delivered to the participant. As a measure of physiological arousal, skin conductance responses were recorded during scanning. Our paradigm allowed us to investigate the role played by the interaction between threat proximity (nearer vs. farther circles), direction (approach vs. retreat), and speed (faster vs. slower) in determining brain responses during anticipatory processing. Importantly, the impact of the factors "proximity" and "speed" were assessed parametrically (i.e., continuously) as they varied dynamically. Therefore, the paradigm allowed us to test how multiple threat-related factors influence signals fluctuations in brain regions. Specifically, do they provide independent response contributions or do they interact in regions important for threat processing, such as the anterior insula, PAG, BNST, and amygdala?

Materials and Methods

Participants

Eighty-five participants (41 females, ages 18-40 years; average: 22.62, STD: 4.85) with normal or corrected-to-normal vision and no reported neurological or psychiatric disease were recruited from the University of Maryland community (of the original sample of 93, data from 7 subjects were discarded due to technical issues during data transfer [specifically, field maps were lost] and 1 other subject was removed because of poor structural-functional alignment). The project was approved by the University of Maryland College Park Institutional Review Board and all participants provided written informed consent before participation. Data from this dataset were analyzed separately at the level of networks and submitted as a separate investigation for publication.

Anxiety questionnaires

Participants completed the trait portion of the Spielberger State-Trait Anxiety Inventory (STAI; Spielberger et al., 1970) about 1-2 weeks before scanning, and then completed the state portion of the STAI immediately before the scanning session.

Experimental Design and Statistical Analysis

Procedure and Stimuli

To create anxious states, two circles with different colors moved around on the screen randomly. When they collided with each other, an unpleasant mild electric shock was delivered. Overall, proximity, direction of movement, and relative speed of the circles were used to influence the threat state. The position of each circle (on the plane), $\boldsymbol{x}_t$, was defined based on its previous position, $\boldsymbol{x}_{t-1}$, plus a random displacement, $\Delta\boldsymbol{x}_t$:

$$\boldsymbol{x}_{\mathrm{t}} = \boldsymbol{x}_{t-1} + \Delta\boldsymbol{x}_t$$

The magnitude and direction of the displacement was calculated by combining a normal random distribution with a momentum term to ensure motion smoothness, while at the same time remaining (relatively) unpredictable to the participants. Specifically, the displacement was updated every 50 ms as follows:

$$\boldsymbol{\Delta x}_t = (1 - c)\boldsymbol{\Delta x}_{t-1} + \ c\mathrm{N}(0,1)$$

where $c = 0.2$ and $\mathrm{N}(0,1)$ indicates the normal distribution with zero mean and standard deviation of 1. The position and amount of displacement of each circle were updated independently.

Visual stimuli were presented using PsychoPy (http://www.psychopy.org/) and viewed on a projection screen via a mirror mounted to the scanner's head coil. The total experiment included 6 runs, each of which had 6 blocks (3/85 participants had only 5 runs). In each block, the circles appeared on the screen and moved around for 60 seconds; blocks were preceded by a 15-second blank screen. Each run ended with a 7-second blank screen.

To ensure that the effects of threat proximity and direction were uncorrelated, half of the blocks in each run were temporally reversed versions of the other blocks in that run. Temporally reversing the stimulus trajectories guarantees that proximity and direction are uncorrelated because reversing time changes the sign of the direction (that is, approach becomes retreat). To optimize the experimental design, 10,000 candidate stimuli trajectories and block orders were generated. We then selected six runs which minimized collinearity between all predictors of interest (see below), measured as the sum of respective variance inflation factors (Neter et al., 1996).

In each run the circles collided eight times within 4 out of 6 blocks (maximum of 3 times in a block); each collision resulted in the delivery of an electric shock. The 500-ms electric shock was delivered by an electric stimulator (Coulbourn Instruments, PA, USA) to the fourth and fifth fingers of the non-dominant left hand via MRI-compatible electrodes. To calibrate the intensity of the shock, each

participant was asked to choose his/her own stimulation level immediately prior to functional imaging, such that the stimulus would be "highly unpleasant but not painful." After each run, participants were asked about the unpleasantness of the stimulus in order to re-calibrate shock strength, if needed. Skin conductance response (SCR) data were collected using the MP-150 system (BIOPAC Systems, Inc., CA, USA) at a sampling rate of 250 Hz by using MRI compatible electrodes attached to the index and middle fingers of the non-dominant left hand. Due to technical problems and/or experimenter errors during data collection, SCR data was not available in two participants, and six participants had only five runs of the SCR data; one participant who had only 3 runs of data was excluded from the analysis.

MRI data acquisition

Functional and structural MRI data were acquired using a 3T Siemens TRIO scanner with a 32-channel head coil. First, a high-resolution T2-weighted anatomical scan using Siemens's SPACE sequence (0.8 mm isotropic) was collected. Subsequently, we collected 457 functional EPI volumes in each run using a multiband scanning sequence (Feinberg et al., 2010) with TR = 1.0 sec, TE = 39 ms, FOV = 210 mm, and multiband factor = 6. Each volume contained 66 non-overlapping oblique slices oriented 30° clockwise relative to the AC-PC axis (2.2 mm isotropic). A high-resolution T1-weighted MPRAGE anatomical scan (0.8 mm isotropic) was collected. Additionally, in each session, double-echo field maps (TE1 = 4.92 ms, TE2 = 7.38 ms) were acquired with acquisition parameters matched to the functional data.

Functional MRI preprocessing

To preprocess the functional and anatomical MRI data, a combination of packages and in-house scripts were used. The first three volumes of each functional run were discarded to account for equilibration effects. Slice-timing correction (with AFNI's 3dTshift) used Fourier interpolation to align the onset times of every slice in a volume to the first acquisition slice, and then a six-parameter rigid body

transformation (with AFNI's 3dvolreg) corrected head motion within and between runs by spatially registering each volume to the first volume.

In this study, we strived to improve functional-anatomical co-registration given the small size of some of the structures of interest. Skull stripping determines which voxels are to be considered part of the brain and, although conceptually simple, plays a very important role in successful subsequent co-registration and normalization steps. Currently, available packages perform sub-optimally in specific cases, and mistakes in the brain-to-skull segmentation can be easily identified. Accordingly, to skull strip the T1 high-resolution anatomical image (which was rotated to match the oblique plane of the functional data with AFNI's 3dWarp), we employed six different packages [ANTs (Avants et al., 2009; http://stnava.github.io/ANTs/), AFNI (Cox, 1996; http://afni.nimh.nih.gov/), ROBEX (Iglesias et al., 2011; https://www.nitrc.org/projects/robex), FSL (Smith et al., 2004; http://fsl.fmrib.ox.ac.uk/fsl/fslwiki/), SPM (http://www.fil.ion.ucl.ac.uk/spm/), and BrainSuite (Shattuck and Leahy, 2002; http://brainsuite.org/)] and employed a "voting scheme" as follows: based on T1 data, a voxel was considered to be part of the brain if four-out-of-six packages estimated it to be a brain voxel; otherwise the voxel was not considered to be brain tissue (for 6 subjects whose T1 data were lost due to issues during data transfer, the T2 image was used instead and only the ANTs package was used for skull-stripping).

Subsequently, FSL was used to process field map images and create a phase-distortion map for each participant (bet and fsl_prepare_fieldmap). FSL's epi_reg was then used to apply boundary-based co-registration to align the unwarped mean volume registered EPI image with the skull-stripped anatomical image (T1 or T2) along with simultaneous EPI distortion-correction (Greve and Fischl, 2009).

Next, ANTS was used to learn a nonlinear transformation that mapped the skull-stripped anatomical image (T1 or T2) to the skull-stripped MNI152 template (interpolated to 1-mm isotropic voxels). Finally, ANTS combined the nonlinear transformations from co-registration/unwarping (from

mapping mean functional EPI image to the anatomical T1 or T2) and normalization (from mapping T1 or T2 to the MNI template) into a single transformation that was applied to map volume registered functional volumes to standard space (interpolated to 2-mm isotropic voxels). In this process, ANTS also utilized the field maps to simultaneously minimize EPI distortion. The resulting spatially normalized functional data was blurred using a 4mm full-width half-maximum (FWHM) Gaussian filter. Spatial smoothing was restricted to grey-matter mask voxels. Finally, intensity of each voxel was normalized to a mean of 100 (separately for each run).

Voxelwise analysis

Each participant's preprocessed functional MRI data were analyzed using multiple linear regression with AFNI (restricted to gray-matter voxels) using the 3dDeconvolve program. Time series data were analyzed according to the following model (nuisance variables are described below):

$$Y = \beta_P P + \beta_D D + \beta_S S + \beta_{PD} PD + \beta_{PS} PS + \beta_{DS} DS + \beta_{PDS} PDS \quad (1)$$

where P indicates proximity, D represents direction, and S represents speed. Terms PD, PS, and PDS represent the interactions terms; the individual terms P, D, and S were mean centered prior to multiplication to reduce potential collinearity (the resulting regressors exhibited pairwise correlations that were small and the largest one was .33; all variance inflation factors were < 1.2). The ßs represent parameter estimates that minimize error. Variables were determined based on circle positions on the screen. Proximity was defined as the Euclidean distance between the two circles; direction indicated approach vs. retreat; speed was the discrete temporal difference of proximity.

For each run, the regressors were obtained by first decimating the 20 Hz sample rate stimuli information (of circles movements) to the fMRI sample rate (1 Hz). In addition to the variables above, we included regressors for visual motion (velocity tangential to the difference vector of the combined circle-to-circle stimulus), sustained block event (60-sec duration), and block-onset and block-offset

events (1-second duration) to account for transient responses at block onset/offset. All regressors were convolved with a standard hemodynamic response based on the gamma-variate model (Cohen, 1997); note that interaction regressors were multiplied prior to convolution. Other regressors included in the model included 6 motion parameters (3 linear displacements and 3 angular rotations), and their discrete temporal derivatives. To further control for head motion-related artifacts in the data (Siegel et al., 2014), we excluded volumes (on average 0.4%) with a frame-to-frame displacement of more than 1 mm. To model baseline and drifts of the MR signal, regressors corresponding to polynomial terms up to 4th order were included (for each run separately). Finally, to minimize effects due to the physical shock event, data points in a 15-sec window after shock delivery were discarded from the analysis.

Group analysis

Whole-brain voxelwise random-effects analyses were conducted using response estimates from individual-level analyses (restricted to gray-matter voxels) in AFNI. To probe the effects of the regressors of interest, we ran separate one-sample *t*-tests against zero using the AFNI's 3dttest++ program.

The alpha-level for voxelwise statistical analysis was determined by simulations using the 3dClustSim program (restricted to gray-matter voxels). For these simulations, the smoothness of the data was estimated using 3dFWHMx program (restricted to gray-matter voxels) based on the residual time series from the individual-level voxelwise analysis. Taking into account the recent report of increased false-positive rates linked to the assumption of Gaussian spatial autocorrelation in fMRI data (Eklund et al., 2016), we used the -acf (i.e., auto-correlation function) option recently added to the 3dFWHMx and 3dClustSim tools, which models spatial fMRI noise as a mixture of Gaussian plus mono-exponential distributions. This improvement was shown to control false positive rates around the desired alpha level, especially with relatively stringent voxel-level uncorrected p-values such as 0.001

(Cox et al., 2017). Based on a voxel-level uncorrected p-value of 0.001, simulations indicated a minimum cluster extent of 13 voxels (2.0 x 2.0 x 2.0 mm) for a cluster-level corrected alpha of 0.05.

BNST ROI analysis

We investigated basal forebrain sites consistent with the BNST. Given that the BNST is a small region and the voxelwise analysis was done on spatially smoothed data, we conducted an additional ROI analysis. Left and right BNST ROIs were defined anatomically according to the probabilistic mask of the BNST (at 25% threshold) recently reported by Blackford and colleagues (Theiss et al., 2017). For this analysis, no spatial smoothing was applied. In each participant, for each ROI, a representative time series was created by averaging the unsmoothed time series from all the gray-matter voxels within the anatomically defined ROI. Then, as in the individual-level voxelwise analysis, multiple linear regression analysis was run using the 3dDeconvolve program to estimate condition-specific responses. At the group level, as in the voxelwise analysis, we ran separate one-sample *t*-test's against zero using the corresponding regression coefficients from the individual-level analysis.

Skin conductance response (SCR) analysis

Each participant's SCR data were initially smoothed with a median-filter over 50 samples (200 ms) to reduce scanner-induced noise. In each run, the first 3 seconds of data was discarded (corresponding to first 3 volumes excluded in the fMRI analysis) and the remaining data were resampled by decimating the 250 Hz sample rate to the sample rate of fMRI data (1 Hz) and subsequently *Z*-scored. The pre-processed SCR data were then analyzed using multiple linear regression using the 3dDeconvolve program in AFNI. For related approaches see Bach et al. (2009) and Engelmann et al. (2015). As in the fMRI data analysis, there were seven main event types in the design matrix (see equation 1). In addition, we included regressors for visual motion (velocity tangential to the difference vector of the combined circle-to-circle

stimulus), sustained block event (60-sec duration), and block-onset and block-offset events (1-second duration) to account for transient responses at block onset/offset. All the regressors were convolved with a standard hemodynamic response based on the gamma-variate model (Cohen, 1997). Additionally, constant and linear terms were included (for each run separately) to model baseline and drifts of the SCR. To minimize effects due to the physical shock event, data points in a 15-sec window after shock delivery were discarded from the analysis. At the group level, to probe the effects of the regressors of interest, we ran separate one-sample *t*-tests against zero using the corresponding regression coefficients from the individual-level analysis.

Relationship between SCR and brain activity

To probe the relationship between brain activity and physiological arousal measured via SCRs, we focused on clusters that exhibited a proximity x direction x speed interaction, which aimed to reduce the multiple-comparisons problem. For each participant and cluster, an interaction index was created by averaging the corresponding regression coefficient (β_{PDS} in equation 1) from all the voxels within the cluster. Then, for each cluster, we ran a robust correlation (Rousselet and Pernet, 2012; Wilcox, 2012) across participants. For each participant, we considered the average fMRI interaction index and the corresponding interaction term in the SCR data (specifically, the coefficient β_{PDS} obtained from the SCR regression analysis).

Contour plots and plotting responses as a function of continuous factors

In Figure 7, estimated brain activation was plotted as a function of proximity which was a continuous factor. To do so, the average (across participants) β coefficients of equation 1 were used and estimated activation was computed for a range of proximity values (that is, fitted responses were obtained by applying equation 1). Both binned and continuous versions of the relationship are shown.

Contour plots in Figure 3 (for SCR) and Figures 9-10 (for fMRI) were obtained in a similar fashion, and estimated responses were plotted as a function of proximity and speed. The range +/- 1 SD for plotting was chosen because it covers the densest part of proximity and speed values employed during actual circle movement (larger and smaller values were relatively less frequent).

Results

The paradigm allowed us to investigate the role played by threat proximity, direction, and speed, and their interactions, on SCR and fMRI responses. Intuitively, interactions evaluated the extent to which "context" mattered (Figure 1C). For instance, the contrast of approach vs. retreat (direction) was anticipated to depend on proximity. Moreover, as proximity and speed varied continuously, their roles and their interactions were assessed parametrically.

Skin Conductance Responses

Analysis of SCR data revealed an effect of direction, where greater responses were observed when circles were approaching compared to retreating from each other (Table 1). All interaction effects were noteworthy. In particular, the interaction of proximity by direction indicates that responses to approach vs. retreat depended on threat distance, such that responses were larger when nearer vs. farther. The three-way interaction indicates that the proximity by direction interaction was also modulated by speed, such that proximity and direction contributions increased at faster speeds. To visualize the three-way interaction, contour plots (with directions of maximal change shown as arrows) are shown for the approach and retreat conditions (Figure 3); the insets show patterns that illustrate potential scenarios with individual effects and interactions. During approach, SCR increased as function of both proximity and speed, but in a way that depended on specific combinations of these factors (that is, not additively; compare the upper-right and lower-left quadrants). However, during retreat, the contributions of

proximity and speed were closer to being additive (they were similar for different proximity and speed values), leading to a 3-way interaction.

fMRI voxelwise analysis

Figures 4-5 (Tables 2-3) show the effects of proximity and direction (Table 4 shows the effect of speed). The main focus of this study was to investigate interactions between threat-related factors. Figure 6 (Table 5) shows interactions between proximity and direction; positive voxels (red) show effects when the contrast of approach vs. retreat was greater during closer vs. farther circles, and blue voxels indicate the opposite. Responses for the right anterior insula are illustrated in Figure 7A (similar responses were observed on the left). When the circles were near each other, a larger approach vs. retreat differential response was observed compared to when the circles were far. Responses for the right amygdala (Figure 7B) exhibited the opposite pattern (similar results were observed in the left amygdala but did not survive cluster thresholding; at $p = .001$ a 4-voxel cluster was present); responses were larger for retreat compared to approach, and the contrast was enhanced when circles were near compared to far. Figure 7C-D shows the same responses for approach and retreat for a range of proximity values, which aids in visualizing the parametric effects of proximity on the signals in the two regions. Tables 6-7 show two-way interactions between direction and speed and between proximity and speed.

Figure 8 shows the three-way interaction of proximity by direction by speed, with effects in the anterior insula, frontal-eye field, PAG, cingulate gyrus, and precentral gyrus (Table 8). As the three factors simultaneously affect responses, the interactions can be visualized via contour plots (Figure 9). Consider the approach case for the right anterior insula (Figure 9A); when proximity increased (circles moved closer), stronger responses were observed as speed increased from slower to faster (compare the upper-right vs. lower-left quadrants). However, during retreat, differential responses to speed

(faster vs. slower) were comparable when circles were nearer and farther leading to a 3-way interaction. Figure 9B-C shows similar patterns for the right PAG and mid-cingulate cortex.

BNST ROI analysis

Given the importance of the BNST in aversive processing, we ran a focused analysis using anatomically defined left/right BNST masks, and unsmoothed data to minimize the influence of signals from surrounding structures. We observed a robust effect of threat proximity in the right BNST (and weak evidence in the left BNST), with stronger responses when circles were closer than farther (Table 9). For the right BNST, some evidence for an effect of speed and proximity by speed interaction were seen. Figure 10 shows contour plots for the right BNST. The proximity by speed interaction is evident by the flow lines pointing to the upper-right corner. Intriguingly, the patterns are relatively similar for approach and retreat, which meshes with the fact that no discernible effect of direction (approach vs. retreat) was observed. Thus, the BNST does not appear to robustly differentiate between approach and retreat in our task, and is engaged as long as there is threat movement (closer > farther).

Relationship between SCR responses and brain activity

We evaluated the linear relationship between SCR and fMRI by running a robust correlation analysis (across subjects). Because multiple aspects of both the SCR and fMRI data could be probed (simple effects and interactions), we chose to focus the interrogation on the three-way interaction. Thus, for both SCR and fMRI, the strength of the three-way interaction was considered for the analysis (as given by the beta coefficient in equation 1). This also allowed us to focus on a relatively small number of clusters exhibiting a three-way interaction (and thus have more statistical power for detection of a relationship). We observed a positive linear relationship in all these regions (Table 10); the most robust ones involved the right PAG and mid-cingulate gyrus (Figure 11).

Individual differences in state and trait anxiety

Linear relationships between state/trait anxiety and SCR or fMRI responses were not detected.

Discussion

Whereas previous studies have focused on determining the effect of individual threat-related factors (Mobbs and colleagues 2010; Somerville and colleagues 2010), threat processing is known to be highly context sensitive and dynamic (Fanselow and Lester, 1988; Blanchard and Blanchard, 1990; Kavaliers and Choleris, 2001; Mobbs et al., 2015). For example, an important factor is threat proximity, which largely determines how prey reacts to predators; another factor is threat direction, as when a predator is approaching vs. retreating. The present dynamic threat paradigm allowed us to investigate the role of threat-related factors and their temporally evolving interactions. Our findings support the view that threat processing is context sensitive and dynamic. Whereas some brain regions tracked individual threat-related factors (proximity, direction, or speed), others were also sensitive to combinations of these variables, including their three-way combination.

Interactions between all threat-related factors investigated here were observed in the anterior insula, frontal eye field, mid-cingulate cortex, supplementary motor area (posterior superior frontal gyrus), precentral gyrus, and midbrain/PAG. In all these regions, responses were jointly affected by proximity and speed in a manner that depended on the direction of threat (approach vs. retreat). Historically, the PAG has been implicated in aversive and defensive reactions (Bandler, 1988; Bandler and Shipley, 1994), is in line with more recent studies (Tovote et al., 2016). Indeed, the virtual tarantula manipulation by Mobbs and colleagues (2010) was particularly effective in engaging this structure (although the activation was very extensive, and thus difficult to localize). In humans, the PAG has been suggested to be involved in negative emotional processing more generally (Lindquist et al., 2012;

Satpute et al., 2013). The anterior insula is a highly functionally diverse region (Anderson et al., 2013) that is involved in cognitive, emotional and motivational processes, and supports subjective emotional awareness (Craig, 2002, 2009). Here, the anterior insula was engaged by individual threat-related factors, in addition to factor interactions. In particular, responses in the anterior insula tracked the three-way combination of proximity, direction, and speed. It should be noted that fluctuations of anterior insula (and other regions) signals following the three-way interaction were not due to its responses to individual factors, or two-factor combinations, given that the correlation of the three-way interaction regressor with other regressors was less than .18 (approximately 3% of shared variance).

In previous studies, we and others have observed amygdala *deactivations* during short and long periods of sustained threat (relative to safe conditions; Choi et al., 2012; McMenamin et al., 2014; Grupe et al., 2016). In paradigms closer to the present one, Somerville and colleagues (2010) suggested a limited role of the amygdala in tracking threat proximity, whereas Mobbs and colleagues (2010) observed amygdala responses that responded to the proximity and direction of threat. In a study involving virtual predators, Mobbs and colleagues (2007) reported increased activation in the dorsal amygdala when threat was near, whereas responses were *stronger* in the inferior-lateral amygdala with distant threats. Here, we observed a proximity by direction interaction, such that the retreat vs. approach contrast was enhanced when the circles were *near* compared to far; this interaction pattern was the opposite of that found in the anterior insula, for instance. Thus, in our task, it appears that the amygdala provided a kind of “safety” indicator, particularly when the circles were near. Interestingly, several other regions exhibited similar behavior, including the posterior-insula.

The role of the BNST in threat processing has gained increased attention in the past two decades (Davis and Whalen, 2001; Shackman and Fox, 2016), especially during conditions involving temporally extended and less predictable threats. Given the small size of the structure and its anatomical location, studying it with functional MRI is particularly challenging. Recently, anatomical masks for both regular

and higher field scanning have been published (Avery et al., 2014; Torrisi et al., 2015; Theiss et al., 2017), which should enhance the reproducibility of published findings. We analyzed BNST data using an anatomical mask and unsmoothed data. This is important because nearly all studies have employed some spatial smoothing which blends BNST signals with those of adjacent territories (beyond the inherent point spread function of imaging itself). In the right BNST, we observed an effect of proximity, speed, and a proximity by speed interaction (the last two effects were less robust as they would not survive correction for the seven tests employed; or 14 if one were to consider both hemispheres). The observed effect of proximity is consistent with previous findings that the BNST responds to threat proximity (independent of direction; Somerville et al., 2010; Mobbs et al., 2010; although the activated region was sufficiently large as to make anatomical localization challenging in the Mobbs et al. study).

The mid-cingulate cortex exhibited a three-way interaction. This region receives projections from the orbitofrontal cortex and insula, has been suggested to coordinate fear and avoidance with skeletomotor activity (Vogt et al., 2013), and to be the confluence of cognitive, emotional, and pain-related signals (Vogt, 2005; Shackman et al., 2011). In a previous study, the mid-cingulate cortex was recruited when participants performed a simple target-detection task following exposure to high-arousal unpleasant stimuli, and responses closely mirrored the pattern of behavioral interference (Pereira et al., 2010; see also Pereira et al., 2006). We suggested that the mid-cingulate cortex may be an important site for the interaction between negatively valenced signals and motor signals, and possibly involved in the implementation of defensive responses, which is consistent with the findings of the present study. In addition to the mid-cingulate cortex, two other sites that are frequently involved in motor-related processing exhibited three-way interactions, namely the supplementary motor area (Roland, 1980; Picard and Strick, 1996) and the precentral gyrus. Together, although no overt behavior was required of the participants in the present study, three regions with notable motor-related properties tracked the simultaneous influence of the threat-related factors manipulated here. Our

findings thus resonate with recent calls for a better understanding of motor-affective integration (Blakemore and Vuilleumier, 2016; Hommel et al., 2017).

The three-way interaction was observed at the junction of the pre-central and superior frontal sulci, where the fontal eye field is located in humans (Beauchamp et al., 2001). The fontal eye field is involved in eye movement and attention, and is frequently engaged in cognitively demanding tasks (Beauchamp et al., 2001; Corbetta and Shulman, 2002; Pessoa et al., 2003). Under a "cognitive" interpretation of the functions of the frontal eye field, the region's responses due to individual threat factors and their interactions may have been linked to attentional processing (it is also possible that eye movements played a role). For instance, closer circles may have been associated with increased attention relative to farther circles, especially during approach. An alternative interpretation is that, in the present study, the frontal eye field tracked the affective significance of the overall stimulus (two-circle combination), and thus its responses were sensitive to the threat-related factors manipulated experimentally. This viewpoint is consistent with the proposed close link between attention and affective processing (Pessoa, 2013).

In the present study, we recorded SCR during fMRI scanning to investigate how threat-related factors influence physiological arousal (SCR was recorded in a separate cohort of participants by Somerville et al., 2010), which allowed us to investigate the link between these two measures during dynamic threat anticipation (Maren, 2007). Paralleling the interaction pattern observed in terms of fMRI responses, we also observed a three-way interaction in the SCR data. Notably, SCR and fMRI interactions were positively correlated in the PAG, mid-cingulate cortex, and anterior insula. This relationship indicates a tighter link between brain responses and physiological arousal, suggesting a more prominent role of these regions during dynamic threat anticipation.

To conclude, we investigated how multiple threat-related factors (proximity, direction, and speed) interact when varied continuously. In particular, we asked whether signal fluctuations in brain

regions track threat-related factors dynamically? If so, to what factor(s) and factor combinations are they sensitive? Multiple regions were sensitive to the combination of all three factors; specifically the anterior insula, frontal eye field, mid-cingulate, supplementary motor area, precentral gyrus, and midbrain/PAG. While some of these areas were anticipated, such as the PAG, the involvement of the motor-related areas, such as the supplementary motor area, may be indicative of motor-affective interactions even in situations where overt action is not required. Other areas previously implicated in threat processing were also engaged. In the right BNST, we observed an effect of proximity, speed, and a proximity by speed interaction (the latter two effects were less robust if we consider the multiple tests investigated). In the right amygdala, we observed a proximity by direction interaction, but in the opposite direction as that found for the anterior insula; retreat responses were stronger than approach responses. Thus, in the context of our task, intriguingly, it appears that the amygdala provided a safety-related response. Overall, our study refines our understanding of the mechanisms involved during aversive anticipation in the human brain. Importantly, it emphasizes that threat processing should be understood in a manner that is both context sensitive and dynamic.

References

Anderson ML, Kinnison J, Pessoa L (2013) Describing functional diversity of brain regions and brain networks. Neuroimage 73:50-58.

Avants BB, Tustison N, Song G (2009) Advanced normalization tools (ANTS). Insight J 2:1-35.

Avery SN, Clauss JA, Winder DG, Woodward N, Heckers S, Blackford JU (2014) BNST neurocircuitry in humans. Neuroimage 91:311-323.

Bach DR, Flandin G, Friston KJ, Dolan RJ (2009) Time-series analysis for rapid event-related skin conductance responses. J Neurosci Methods 184:224-234.

Bandler R (1988) Brain mechanisms of aggression as revealed by electrical and chemical stimulation: Suggestion of a central role for the midbrain periaqueductal grey region. Progress in Psychobiology and Physiological Psychology 13:67-154.

Bandler R, Shipley MT (1994) Columnar organization in the midbrain periaqueductal gray: modules for emotional expression? Trends Neurosci 17:379-389.

Beauchamp MS, Petit L, Ellmore TM, Ingeholm J, Haxby JV (2001) A parametric fMRI study of overt and covert shifts of visuospatial attention. Neuroimage 14:310-321.

Blakemore RL, Vuilleumier P (2016) An emotional call to action: Integrating affective neuroscience in models of motor control. Emotion Review:1754073916670020.

Blanchard DC, Griebel G, Pobbe R, Blanchard RJ (2011) Risk assessment as an evolved threat detection and analysis process. Neurosci Biobehav Rev 35:991-998.

Blanchard RJ, Blanchard DC (1990) Anti-predator defense as models of animal fear and anxiety.

Choi JM, Padmala S, Pessoa L (2012) Impact of state anxiety on the interaction between threat monitoring and cognition. Neuroimage 59:1912-1923.

Cohen MS (1997) Parametric analysis of fMRI data using linear systems methods. Neuroimage 6:93-103.

Corbetta M, Shulman GL (2002) Control of goal-directed and stimulus-driven attention in the brain. Nat Rev Neurosci 3:201-215.

Cox RW (1996) AFNI: Software for analysis and visualization of functional magnetic resonance neuroimages. Computers and Biomedical Research 29:162-173.

Cox RW, Chen G, Glen DR, Reynolds RC, Taylor PA (2017) FMRI Clustering in AFNI: False-Positive Rates Redux. Brain Connect 7:152-171.

Craig AD (2002) How do you feel? Interoception: the sense of the physiological condition of the body. Nat Rev Neurosci 3:655-666.

Craig AD (2009) How do you feel--now? The anterior insula and human awareness. Nat Rev Neurosci 10:59-70.

Davis M, Whalen PJ (2001) The amygdala: Vigilance and emotion. Molecular Psychiatry 6:13-34.

Dillon DG, Rosso IM, Pechtel P, Killgore WD, Rauch SL, Pizzagalli DA (2014) Peril and pleasure: an rdoc-inspired examination of threat responses and reward processing in anxiety and depression. Depress Anxiety 31:233-249.

Eklund A, Nichols TE, Knutsson H (2016) Cluster failure: Why fMRI inferences for spatial extent have inflated false-positive rates. Proceedings of the National Academy of Sciences:201602413.

Engelmann JB, Meyer F, Fehr E, Ruff CC (2015) Anticipatory anxiety disrupts neural valuation during risky choice. J Neurosci 35:3085-3099.

Fanselow MS, Lester LS (1988) A functional behavioristic approach to aversively motivated behavior: Predatory imminence as a determinant of the topography of defensive behavior.

Fanselow MS, & Lester, L. S. (1988) A functional behavioristic approach to aversively motivated behavior: Predatory imminence as a determinant of the topography of defensive behavior. Evolution and Learning:185-212.

Feinberg DA, Moeller S, Smith SM, Auerbach E, Ramanna S, Glasser MF, Miller KL, Ugurbil K, Yacoub E (2010) Multiplexed echo planar imaging for sub-second whole brain FMRI and fast diffusion imaging. PloS One 5:e15710.
Greve DN, Fischl B (2009) Accurate and robust brain image alignment using boundary-based registration. Neuroimage 48:63-72.
Grupe DW, Nitschke JB (2013) Uncertainty and anticipation in anxiety: an integrated neurobiological and psychological perspective. Nat Rev Neurosci 14:488-501.
Grupe DW, Oathes DJ, Nitschke JB (2013) Dissecting the anticipation of aversion reveals dissociable neural networks. Cereb cortex 23:1874-1883.
Grupe DW, Wielgosz J, Davidson RJ, Nitschke JB (2016) Neurobiological correlates of distinct post-traumatic stress disorder symptom profiles during threat anticipation in combat veterans. Psychol Med 46:1885-1895.
Hommel B, Moors A, Sander D, Deonna J (2017) Emotion meets action: towards an integration of research and theory. Emotion Review:1754073916689379.
Iglesias JE, Liu C-Y, Thompson PM, Tu Z (2011) Robust brain extraction across datasets and comparison with publicly available methods. IEEE Trans Med Imaging 30:1617-1634.
Jensen J, McIntosh AR, Crawley AP, Mikulis DJ, Remington G, Kapur S (2003) Direct activation of the ventral striatum in anticipation of aversive stimuli. Neuron 40:1251-1257.
Kavaliers M (2001) Antipredator responses and defensive behavior: ecological and ethological approaches for the neurosciences. Neurosci Biobehav Rev 25:577-586.
Kavaliers M, Choleris E (2001) Antipredator responses and defensive behavior: ecological and ethological approaches for the neurosciences. Neurosci Biobehav Rev 25:577-586.
Lindquist KA, Wager TD, Kober H, Bliss-Moreau E, Barrett LF (2012) The brain basis of emotion: a meta-analytic review. Behav Brain Sci 35:121-143.
Maren S (2007) Neuroscience. The threatened brain. Science 317:1043-1044.
McMenamin BW, Langeslag SJ, Sirbu M, Padmala S, Pessoa L (2014) Network organization unfolds over time during periods of anxious anticipation. J Neurosci 34:11261-11273.
Mobbs D, Hagan CC, Dalgleish T, Silston B, Prévost C (2015) The ecology of human fear: survival optimization and the nervous system. Front Neurosci 9.
Mobbs D, Yu R, Rowe JB, Eich H, FeldmanHall O, Dalgleish T (2010) Neural activity associated with monitoring the oscillating threat value of a tarantula. Proc Natl Acad Sci USA 107:20582-20586.
Mobbs D, Petrovic P, Marchant JL, Hassabis D, Weiskopf N, Seymour B, Dolan RJ, Frith CD (2007) When fear is near: threat imminence elicits prefrontal-periaqueductal gray shifts in humans. Science 317:1079-1083.
Neter J, Kutner MH, Nachtsheim CJ, Wasserman W (1996) Applied linear statistical models (4th edition), Fourth edition Edition. Chicago: Irwin.
Pereira MG, Volchan E, de Souza GG, Oliveira L, Campagnoli RR, Pinheiro WM, Pessoa L (2006) Sustained and transient modulation of performance induced by emotional picture viewing. Emotion 6:622-634.
Pereira MG, de Oliveira L, Erthal FS, Joffily M, Mocaiber IF, Volchan E, Pessoa L (2010) Emotion affects action: Midcingulate cortex as a pivotal node of interaction between negative emotion and motor signals. Cogn Affect Behav Neurosci 10:94-106.
Pessoa L (2013) The Cognitive-Emotional Brain: From Interactions to Integration. Cambridge: MIT Press.
Pessoa L, Kastner S, Ungerleider LG (2003) Neuroimaging studies of attention: From modulation of sensory processing to top-down control. J Neurosci 23:3990-3998.
Picard N, Strick PL (1996) Motor areas of the medial wall: a review of their location and functional activation. Cereb cortex 6:342-353.

Roland PE, Larsen, B., Lassen, N. A., Skinhoj, E. (1980) Supplementary motor area and other cortical areas in organization of voluntary movements in man. J Nuerophysiol 43:118-136.
Rousselet GA, Pernet CR (2012) Improving standards in brain-behavior correlation analyses. Front Hum Neurosci 6:119.
Satpute AB, Wager TD, Cohen-Adad J, Bianciardi M, Choi JK, Buhle JT, Wald LL, Barrett LF (2013) Identification of discrete functional subregions of the human periaqueductal gray. Proc Natl Acad Sci U S A 110:17101-17106.
Shackman AJ, Fox AS (2016) Contributions of the Central Extended Amygdala to Fear and AnxietyContributions of the Central Extended Amygdala to Fear and Anxiety. J Neurosci 36:8050-8063.
Shackman AJ, Salomons TV, Slagter HA, Fox AS, Winter JJ, Davidson RJ (2011) The integration of negative affect, pain and cognitive control in the cingulate cortex. Nat Rev Neurosci 12:154-167.
Shattuck DW, Leahy RM (2002) BrainSuite: an automated cortical surface identification tool. Medical image analysis 6:129-142.
Siegel JS, Power JD, Dubis JW, Vogel AC, Church JA, Schlaggar BL, Petersen SE (2014) Statistical improvements in functional magnetic resonance imaging analyses produced by censoring high-motion data points. Hum Brain Mapp 35:1981-1996.
Simmons A, Strigo I, Matthews SC, Paulus MP, Stein MB (2006) Anticipation of aversive visual stimuli is associated with increased insula activation in anxiety-prone subjects. Biol Psychiatry 60:402-409.
Smith SM, Jenkinson M, Woolrich MW, Beckmann CF, Behrens TE, Johansen-Berg H, Bannister PR, De Luca M, Drobnjak I, Flitney DE, Niazy RK, Saunders J, Vickers J, Zhang Y, De Stefano N, Brady JM, Matthews PM (2004) Advances in functional and structural MR image analysis and implementation as FSL. Neuroimage 23 Suppl 1:S208-219.
Somerville LH, Whalen PJ, Kelley WM (2010) Human bed nucleus of the stria terminalis indexes hypervigilant threat monitoring. Biol Psychiatry 68:416-424.
Spielberger CD, Gorsuch RL, Lushene RE (1970) Manual for the State-Trait Anxiety Inventory. Palo Alto, CA: Consulting Psychologists Press.
Theiss JD, Ridgewell C, McHugo M, Heckers S, Blackford JU (2017) Manual segmentation of the human bed nucleus of the stria terminalis using 3T MRI. Neuroimage 146:288-292.
Torrisi S, O'Connell K, Davis A, Reynolds R, Balderston N, Fudge JL, Grillon C, Ernst M (2015) Resting state connectivity of the bed nucleus of the stria terminalis at ultra-high field. Hum Brain Mapp 36:4076-4088.
Tovote P, Esposito MS, Botta P, Chaudun F, Fadok JP, Markovic M, Wolff SB, Ramakrishnan C, Fenno L, Deisseroth K, Herry C, Arber S, Luthi A (2016) Midbrain circuits for defensive behaviour. Nature 534:206-212.
Vogt BA (2005) Pain and emotion interactions in subregions of the cingulate gyrus. Nat Rev Neurosci 6:533-544.
Vogt J, De Houwer J, Crombez G, Van Damme S (2013) Competing for attentional priority: temporary goals versus threats. Emotion 13:587-598.
Vytal KE, Overstreet C, Charney DR, Robinson OJ, Grillon C (2014) Sustained anxiety increases amygdala–dorsomedial prefrontal coupling: a mechanism for maintaining an anxious state in healthy adults. Journal of psychiatry & neuroscience: JPN 39:130145.
Wilcox RR (2012) Introduction to robust estimation and hypothesis testing: Academic Press.
Woo CW, Krishnan A, Wager TD (2014) Cluster-extent based thresholding in fMRI analyses: Pitfalls and recommendations. Neuroimage.

Figure Legends

Figure 1. Threat-related factors and their interaction. (A) Closer and farther threat (represented by the snake). (B) Direction of threat: approach vs. retreat. (C) Threat level may depend on both proximity (closer and farther) and direction (left panels indicate approach; right panels indicate retreat).

Figure 2. Experimental paradigm. Two circles moved randomly on the screen and a shock was administered to the participant if they touched. The inset represents threat proximity (the distance between the two circles), which varied continuously. A central goal of the study was to determine the extent to which signal fluctuations in brain regions (such as the anterior insula) followed threat-related factors (including proximity) and their interactions.

Figure 3. Skin conductance response (SCR) as a function of proximity and speed. Contour plot shows estimated SCR response for different combinations of proximity and speed. Estimated response strength is indicated by color (bands of the same color have responses in the same range). Arrows indicate direction of maximal change in SCR response; green arrows indicate direction of response increase and white arrows indicate direction of response decrease. The inset illustrates how to interpret the contour plots (arrows indicate direction of response increase). During approach segments, SCR increased for higher proximity (circles closer to each other) and higher speeds, particularly when closer and at higher speeds. A.U.: arbitrary units.

Figure 4. Brain responses as a function of threat proximity. Clusters in red show regions with stronger responses for closer vs. farther (see inset); clusters in blue show the reverse. SMA: supplementary motor area; FEF: frontal eye field; MCC: mid-cingulate cortex; SFG: superior frontal gyrus; IPS: intraparietal sulcus; PCC: posterior cingulate cortex; vmPFC: ventro-medial prefrontal cortex.

Figure 5. Brain responses as a function of direction (approach vs. retreat). Clusters in red show regions with stronger responses for approach vs. retreat (see inset); clusters in blue show the reverse. PAG: periaqueductal gray; SMA: supplementary motor area; FEF: frontal eye field; PreCG: precentral gyrus; IPS: intraparietal sulcus.

Figure 6. Brain responses exhibiting a proximity by direction (approach vs. retreat) interaction. Clusters in red show regions with approach vs. retreat responses greater when closer vs. farther (see inset); clusters in blue show the reserve pattern. FEF: frontal eye field; PreCG: precentral gyrus.

Figure 7. Illustration of proximity by direction (approach vs. retreat) interaction. (A-B) Proximity was binned in terms of “far” (1/3 farthest) and “near” (1/3 nearest). The box-and-whisker plots show the interquartile range and 1.5 times the range. The final bar plots interaction scores with their within-subject variability. (C-D) Estimated responses for a range of proximity values. For the right anterior insula, the contrast (approach – retreat) was greater when near vs. far. For the right amygdala, responses were larger for retreat vs. approach and difference greatest when “near”. Note that the cross-over pattern in (D) is not observed in (B) because the binning in the latter pools together a range of proximities. The confidence bands were obtained by considering the within-subject differences (approach minus retreat). A.U.: arbitrary units.

Figure 8. Brain responses exhibiting a proximity by direction (approach vs. retreat) by speed interaction. Clusters in red show regions with responses sensitive to all three factors simultaneously. PAG: periaqueductal gray; SMA: supplementary motor area; FEF: frontal eye field; MCC: mid-cingulate cortex

Figure 9. Brain responses as a function of threat-related factors in the right anterior insula (A), right PAG (B) and mid-cingulate cortex (C). Contour plots show estimated fMRI responses for different combinations of proximity and speed, separately for approach and retreat (see Figure 3 for additional explanation). Arrows point in the direction of signal increase for approach and signal decrease for retreat. During approach, both proximity and speed simultaneously influence responses, which increase when the circles are closer and speed is higher. A different pattern is observed for retreat, hence the three-way interaction. During retreat, for the right anterior insula, responses were weakest when the circles were farther from each other. A.U.: arbitrary units.

Figure 10. Brain responses as a function of threat-related factors for the BNST. Contour plots show estimated fMRI responses for different combinations of proximity and speed, separately for approach and retreat (see Figures 3 and 9 for additional explanation). During both approach and retreat, responses were strongest when the circles were closer from each other and speed was high. A.U.: arbitrary units.

Figure 11. Relationship between fMRI signals and skin conductance responses (SCR) in the right PAG (A) and mid-cingulate cortex (B). For both fMRI and SCR, the strength of the three-way interaction was considered for the analysis. Data points correspond to participants. Circles in red were deemed to be outliers based on the robust correlation algorithm.

Table 1. Skin conductance response results.

Regressor	t(81)	p-value
Proximity	-0.74	0.4590
Direction	2.98	0.0038
Speed	1.35	0.1821
DirectionXSpeed	3.83	0.0003
ProximityXDirection	2.56	0.0124
ProximityXSpeed	2.04	0.0444
ProximityXDirectionXSpeed	2.59	0.0115

For reference: 0.05/7 = 0.0071

Table 2. Clusters that exhibited the effect of proximity in voxelwise analysis (peak MNI coordinates, t(84) values, and cluster size [k]). Peak coordinates are presented for completeness and potential meta-analysis; with cluster-based thresholding, it is not possible to conclude that all the reported peaks were activated [see Woo et al., 2014]

k	*x*	*y*	*z*	*t*	*Cluster*
13001	-14	-88	28	-12.08	Occipital cortex/Cuneus/Posterior Cingulate cortex
1572	-24	-94	2	9.11	left Occipital/Temporal gyrus
1556	36	22	8	7.76	right anterior/mid-Insula
1404	30	-8	58	7.29	right Pre-Central sulcus/Superior Frontal/Cingulate gyrus
907	64	-38	30	7.87	right Supramarginal gyrus
847	-14	-72	-24	7.38	left Cerebellum
802	-38	14	4	7.04	left anterior/mid-Insula
558	40	-36	52	6.18	right Inferior Parietal cortex
537	-54	-34	36	6.59	left Supramarginal gyrus
478	8	-18	4	6.87	right/left Thalamus
417	-36	-50	50	3.64	left Inferior Parietal cortex
378	-2	-46	-10	-5.59	ventro-medial PFC
361	-12	-72	-42	6.45	left Cerebellum
308	-34	-6	52	5.51	left Frontal eye field
257	-22	26	46	-5.01	left Superior Frontal gyrus
165	24	32	46	-4.59	right Superior Frontal gyrus
130	-4	-20	30	5.2	right/left posterior Cingulate cortex
79	-34	48	28	4.72	left Superior Frontal gyrus
78	42	-58	-30	5.79	right Cerebellum
66	-24	14	-2	4.99	left Putamen
56	2	34	48	4.79	medial Superior Frontal gyrus
52	58	-4	-18	-4.76	right Middle Temporal gyrus
52	4	14	-10	-5.71	Subcollosal area
51	26	-68	-24	4.81	right Cerebellum
44	12	4	10	4.78	right dorsal Caudate
38	26	42	22	4.89	right Superior Frontal gyrus
37	12	-74	-40	5.87	right Cerebellum
33	-62	-6	-18	-4.41	left Middle Temporal gyrus
33	50	-32	-4	4.58	right Superior Temporal gyurs
31	32	42	-10	-4.83	right lateral Orbitofrontal cortex
30	-4	-66	52	-4.54	Precuneus
25	30	-70	32	4.45	right Parieto-occipitalis
21	18	18	8	4.8	right dorsal Caudate

20	30	-56	-28	4.37	right Cerebellum
20	-16	64	14	4.53	right Superior Frontopolar gyrus
20	-12	-26	36	4.43	left posterior-Cingulate cortex
18	-26	62	-12	4.41	left frontomarginal gyrus
15	12	12	0	4.96	right ventral Caudate
15	-8	18	36	4.59	left mid-Cingulate cortex
14	-28	-36	-34	5.25	left anterior Cerebellum
14	-24	-74	32	3.91	left Parieto-occipitalis
13	18	-76	-22	4.28	right Cerebellum
13	-22	-18	-20	-3.97	left Hippocampus
13	28	-18	-14	-4.61	right Hippocampus
13	18	6	18	4.44	right dorso-lateral Caudate

Table 3. Clusters that exhibited the effect of direction in voxelwise analysis (peak MNI coordinates, t(84) values, and cluster size [k]). Peak coordinates are presented for completeness and potential meta-analysis; with cluster-based thresholding, it is not possible to conclude that all the reported peaks were activated [see Woo et al., 2014]

k	*x*	*y*	*z*	*t*	*Cluster*
817	-34	-42	50	6.97	left Inferior Parietal cortex
805	34	-50	62	6.87	right Inferior Parietal cortex
789	46	-58	10	6.58	right Middle Temporal gyrus
612	-24	-8	52	8.23	left Frontal eye field
572	36	-4	50	7.78	right Frontal eye field
546	-46	-64	12	7.04	left Middle Temporal gyrus
349	36	28	4	7.88	right anterior Insula
321	8	-74	0	-7.09	right Lingual gyrus
276	54	6	36	6.32	right Precentral gyrus
273	16	-88	28	-6.6	right Occipital gyrus
271	-16	-76	-8	-7.35	left Lingual gyrus
267	-22	-24	62	-5.88	left Precentral gyrus
219	-26	-72	26	7.45	left Parieto-occipitalis
216	-12	-94	16	-6.6	left Occipital gyrus
174	-36	18	8	6.69	left anterior Insula
154	-52	2	38	7.53	left Precentral gyrus
149	24	-94	0	-5.52	right Occipital gyrus
115	30	-74	38	5.47	right Parieto-occipitalis
81	22	-24	62	-4.92	right Precentral gyrus
65	2	-28	-2	5.19	right/left Periaqueductal gray (PAG)
59	12	4	70	4.54	right Superior frontal gyrus
58	-10	-72	-42	5.91	left Cerebellum
52	14	-70	-20	6.42	right Cerebellum
49	-44	-70	42	-5.17	left angular gyrus
42	36	-14	44	-5.28	right Postcentral gyrus
41	4	12	58	5.33	right Supplementary Motor Area
37	-14	-72	-22	5.43	left Cerebellum
34	-26	-98	-6	-4.6	left Occipital gyrus
34	-8	-76	-2	-5.52	left Lingual gyrus
28	-22	-34	68	-5.1	left Postcentral gyrus
25	-36	-64	-24	4.71	left Cerebellum
25	-12	-22	40	4.52	left posterior Cingulate cortex
22	52	-32	32	4.37	right Supramarginal gyrus
21	10	-72	-38	5.2	right Cerebellum
20	14	-70	22	-4.46	right Precuneus

19	-38	-16	16	-3.93	left posterior Insula
18	-40	-54	-16	4.45	left Fusiform gyrus
17	-14	-46	-48	4.11	left Cerebellum
17	0	-58	-38	4.08	Cerebellum
17	-12	-46	50	4.39	left Superior Parietal lobule
15	44	-46	-14	4.45	right Fusiform gyrus
13	1	14	-6	4.75	right Putamen
13	-14	-74	18	-4.03	left Occipital gyrus

Table 4. Clusters that exhibited the effect of speed in voxelwise analysis (peak MNI coordinates, t(84) values, and cluster size [k]). Peak coordinates are presented for completeness and potential meta-analysis; with cluster-based thresholding, it is not possible to conclude that all the reported peaks were activated [see Woo et al., 2014]

k	*x*	*y*	*z*	*t*	*Cluster*
2874	48	-68	4	9.09	right Middle Temporal gyrus/Parieto-occipitalis
2430	-46	-74	0	8.73	left Middle Temporal gyrus
390	28	-50	54	6.33	right Intraparietal sulcus
382	-12	-90	2	6.11	left/right Striate cortex
316	-34	-54	60	3.46	left Intraparietal sulcus
215	-32	24	6	5.18	left Anterior Insula
211	-26	-8	56	4.69	left Frontal eye fields
145	-24	-80	30	7.27	left Parieto-occipitalis
125	36	-4	50	5.37	right Frontal eye fields
112	60	-38	22	4.52	right Supramarginal gyrus
103	36	24	6	5.24	right anterior Insula
56	-50	4	36	5.82	left Precentral gyrus
53	-14	-26	38	5.29	left posterior Cingulate cortex
48	48	4	42	4.46	right Precentral gyrus
46	10	-78	-6	6.95	right Lingual gyrus
46	14	10	68	5	right Superior Frontal gyrus
31	-28	56	2	-4.13	left Middle Frontal gyrus
31	-10	16	36	4.43	left mid-Cingulate cortex
29	-58	-40	34	4.44	left Supramarginal gyrus
28	-8	-72	-38	5.55	left Cerebellum
24	8	-54	50	4.55	right Precuneus
22	22	-70	56	4.09	right Superior Parietal lobule
21	-2	52	-4	-3.86	ventro-medial Prefrontal Cortex
20	6	12	56	4.58	right Supplementary Motor Area
19	-26	-44	-8	-4.46	left Parahippocampal gyrus
17	-6	40	-10	-4.25	ventro-medial Prefrontal Cortex
15	68	-30	26	4.29	right Supramarginal gyrus
13	34	-94	16	4.43	right Occipital gyrus

Table 5. Clusters that exhibited the proximity x direction interaction in voxelwise analysis (peak MNI coordinates, t(84) values, and cluster size [k]). Peak coordinates are presented for completeness and potential meta-analysis; with cluster-based thresholding, it is not possible to conclude that all the reported peaks were activated [see Woo et al., 2014]

k	*x*	*y*	*z*	*t*	*Cluster*
1501	10	-74	-2	-9.09	left/right Occipital cortex
578	16	-94	14	-6.27	right Occipital gyrus
271	-40	-20	60	-5.8	left Precentral gyrus
249	-54	-32	-2	-4.88	left Superior Temporal gyrus
225	38	-4	48	6.92	right Frontal eye fields
207	-18	-86	24	-6.53	left Occipital gyrus
166	-20	-10	60	5.36	left Frontal eye field
146	-48	-22	18	-5.31	left Posterior Insula
95	-54	24	16	-4.97	left Inferior Frontal gyrus
80	36	24	8	5.4	right Anterior Insula
79	50	-26	12	-4.29	right Posterior Insula
68	20	-24	70	-4.51	right Precentral gyrus
65	-44	-58	52	-5.5	left angular gyrus
62	26	-72	28	4.84	right Parieto-occipitalis
62	-52	0	38	5.07	left Precentral gyrus
59	40	-14	44	-4.47	right Precentral gyrus
43	50	-28	58	-4.36	right Postcentral gyrus
42	18	-74	24	-4.93	right Precuneus
40	-20	40	42	-4.75	left Superior frontal gyrus
31	-8	-92	16	-5.79	left Occipital gyrus
31	4	-34	54	-4.46	Paracentral lobule
28	34	-22	20	-5.43	right posterior Insula
26	-34	18	8	5.26	left anterior Insula
24	12	-96	6	-4.73	right Occipital gyrus
20	34	-76	-36	-4.21	right Cerebellum
20	48	12	-24	-4.28	right Middle Temporal gyrus
20	-28	-38	-18	-5.35	left Parahippocampal gyrus
20	12	-76	32	-4.44	right Precuenus
15	-28	56	2	-4.2	left middle frontal gyrus
15	-48	-14	52	-4.23	left Postcentral gyrus
14	24	-4	-20	-4.35	right lateral Amygdala

Table 6. Clusters that exhibited the direction x speed interaction in voxelwise analysis (peak MNI coordinates, t(84) values, and cluster size [k]). Peak coordinates are presented for completeness and potential meta-analysis; with cluster-based thresholding, it is not possible to conclude that all the reported peaks were activated [see Woo et al., 2014]

k	*x*	*y*	*z*	*t*	*Cluster*
250	34	26	0	6.87	right Anterior Insula
229	-36	-42	52	6.03	left Inferior Parietal cortex
197	-4	10	50	5.29	Supplementary Motor Area
169	-30	24	6	6.07	left Anterior Insula
143	34	-94	-10	-5.41	right inferior Occipital gyrus
132	-46	-74	0	5.15	left Middle Temporal gyrus
112	-28	-98	-2	-5.17	left inferior Occipital gyrus
101	38	-4	54	5.26	right Frontal eye field
85	-36	-4	48	5.02	left Frontal eye field
73	-48	-66	12	4.65	left Superior Temoporal gyrus
61	14	-72	-2	-5.15	right lingual gyrus
54	-50	2	36	5.2	left Precentral gyrus
37	-42	-60	-12	4.79	left Inferior Temporal gyrus
35	-40	-74	-6	4.36	left Inferior Temporal gyrus
33	10	-80	18	-4.9	right Precuneus
32	12	-78	4	-4.31	right Occipital gyrus
31	-5	26	30	5.04	left mid-Cingulate cortex
28	-4	-32	16	5.72	left Periaqueductal gray (PAG)
28	34	-36	52	4.17	right Inferior Parietal cortex
24	18	-10	64	4.42	right Superior Frontal gyrus
23	42	10	28	4.42	right Inferior Frontal gyrus
21	0	6	32	4.36	mid-Cingulate cortex
21	18	10	64	4.52	right Superior Frontal gyrus
20	-6	-74	40	4.3	left Precuneus
19	-28	-24	52	-4.47	left Precentral gyrus
18	6	-24	0	4.63	right Thalamus
18	-10	36	22	4.47	left anterior-Cingulate cortex
17	8	-14	14	4.45	right Thalamus
17	42	-64	18	3.84	right Superior Temporal gyrus
16	6	-28	-12	4.43	right Periaqueductal gray (PAG)
16	18	-60	28	4.14	right Precuneus
16	-14	6	64	4.34	left Superior Frontal gyrus
15	24	-82	26	-4.37	right Occipital gyrus
13	-12	0	66	3.91	left Superior Frontal gyrus

Table 7. Clusters that exhibited the proximity x speed interaction in voxelwise analysis (peak MNI coordinates, t(84) values, and cluster size [k]). Peak coordinates are presented for completeness and potential meta-analysis; with cluster-based thresholding, it is not possible to conclude that all the reported peaks were activated [see Woo et al., 2014]

k	*x*	*y*	*z*	*t*	*Cluster*
20	8	-76	0	4.02	right Lingual gyrus
14	-18	-94	12	4.06	left Occipital gyrus

Table 8. Clusters that exhibited the proximity x direction x speed interaction in voxelwise analysis (peak MNI coordinates, t(84) values, and cluster size [k]). Peak coordinates are presented for completeness and potential meta-analysis; with cluster-based thresholding, it is not possible to conclude that all the reported peaks were activated [see Woo et al., 2014]

k	*x*	*y*	*z*	*t*	*Cluster*
56	32	28	0	4.65	right Anterior Insula
49	-32	28	0	4.63	left Anterior Insula
43	-56	4	40	4.71	left precentral gyrus
32	-8	4	54	4.21	Supplementary Motor area
31	28	-2	50	4.65	right Superior Frontal gyrus
18	8	-28	-4	4.79	right Periaqueductal gray (PAG)
15	24	-14	56	4.83	right Frontal eye field
13	-4	12	40	4.17	mid-Cingulate cortex
13	-22	0	60	4.08	left Superior Frontal gyrus

Table 9. BNST ROI analysis results.

	Left BNST		Right BNST	
Regressor	**t(84)**	**p-value**	**t(84)**	**p-value**
Proximity	1.76	0.0821	3.70	0.0004
Direction	1.07	0.2863	0.82	0.4155
Speed	-0.43	0.6693	2.18	0.0324
DirectionXSpeed	-0.12	0.9078	0.91	0.3649
ProximityXDirection	-0.75	0.4580	-0.11	0.9113
ProximityXSpeed	-0.55	0.5839	2.26	0.0263
ProximityXDirectionXSpeed	-0.70	0.4889	-1.25	0.2141

For reference: 0.05/7 = 0.0071

Table 10. Relationship between SCR and fMRI activity in clusters that exhibited 3-way interaction.

Region	R	p-value
Right PAG	0.39	0.0003
MCC	0.36	0.0008
Right AI	0.30	0.0061
Left AI	0.28	0.0097
SMA	0.28	0.0101
Right SFG	0.25	0.0216
Left PreCG	0.20	0.0791
Right FEF	0.20	0.0781
Left SFG	0.19	0.0889

For reference: 0.05/9 = 0.0056

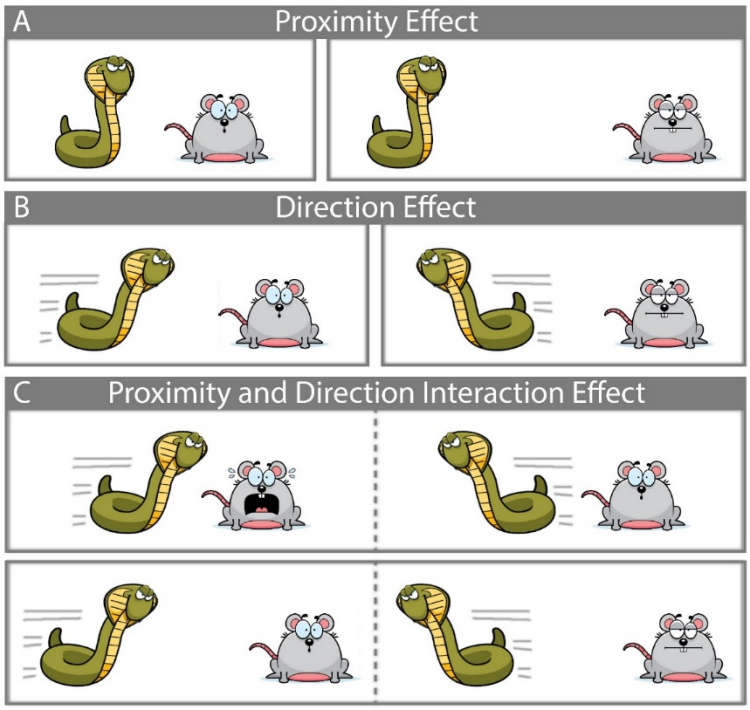
A
Proximity Effect
B
Direction Effect
C
Proximity and Direction Interaction Effect

Figure 1

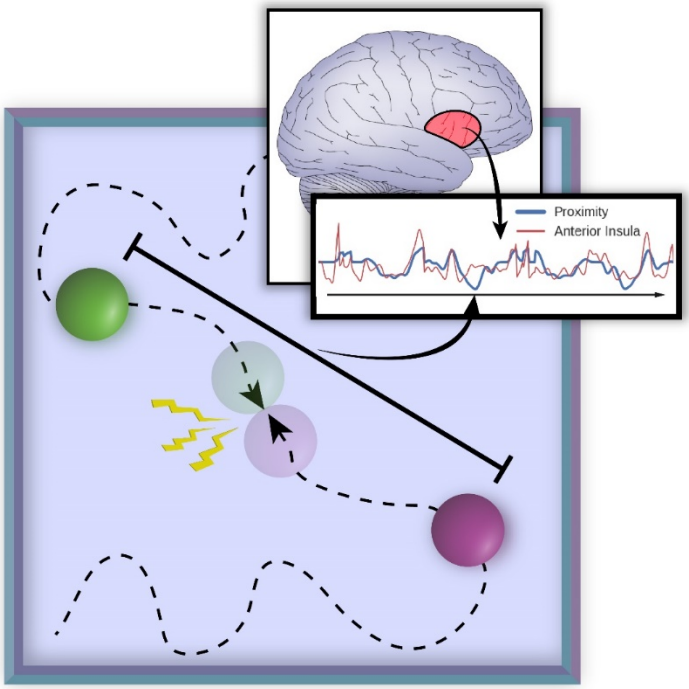

Figure 2

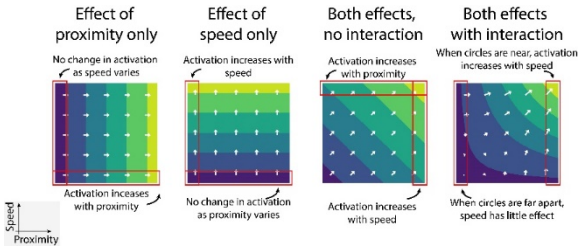
Effect of proximity only
Effect of speed only
Both effects, no interaction
Both effects with interaction
No change in activation as speed varies
Activation increases with speed
Activation increases with proximity
When circles are near, activation increases with speed
Activation inceases with proximity
No change in activation as proximity varies
Activation increases with speed
When circles are far apart, speed has little effect
Speed
Proximity

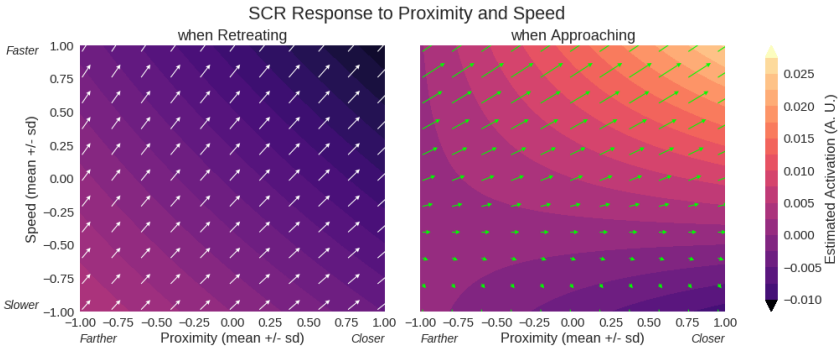
SCR Response to Proximity and Speed
when Retreating
when Approaching
Faster
Slower
Speed (mean +/- sd)
1.00
0.75
0.50
0.25
0.00
−0.25
−0.50
−0.75
−1.00
Farther
Proximity (mean +/- sd)
Closer
Estimated Activation (A. U.)
0.025
0.020
0.015
0.010
0.005
0.000
−0.005
−0.010

Figure 3

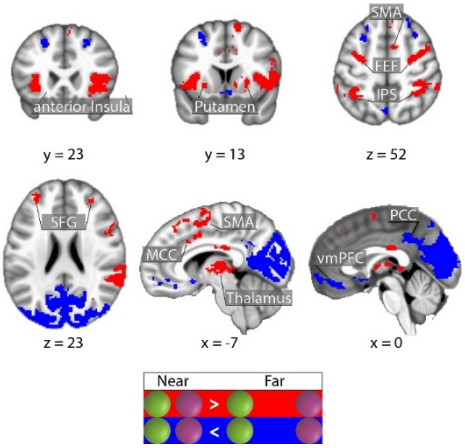
SMA
FEF
IPS
anterior Insula
Putamen
y = 23
y = 13
z = 52
SFG
SMA
PCC
MCC
vmPFC
Thalamus
z = 23
x = -7
x = 0
Near
Far
>
<

Figure 4

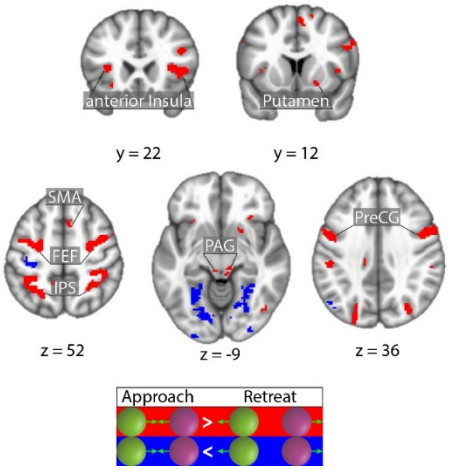
anterior Insula
Putamen
y = 22
y = 12
SMA
FEF
IPS
PAG
PreCG
z = 52
z = -9
z = 36
Approach
Retreat
>
<

Figure 5

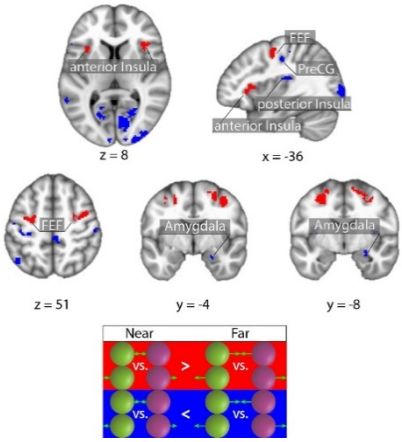
anterior Insula
z = 8
FEF
PreCG
posterior Insula
anterior Insula
x = -36
FEF
z = 51
Amygdala
y = -4
Amygdala
y = -8
Near
Far
vs.
>
vs.
vs.
<
vs.

Figure 6

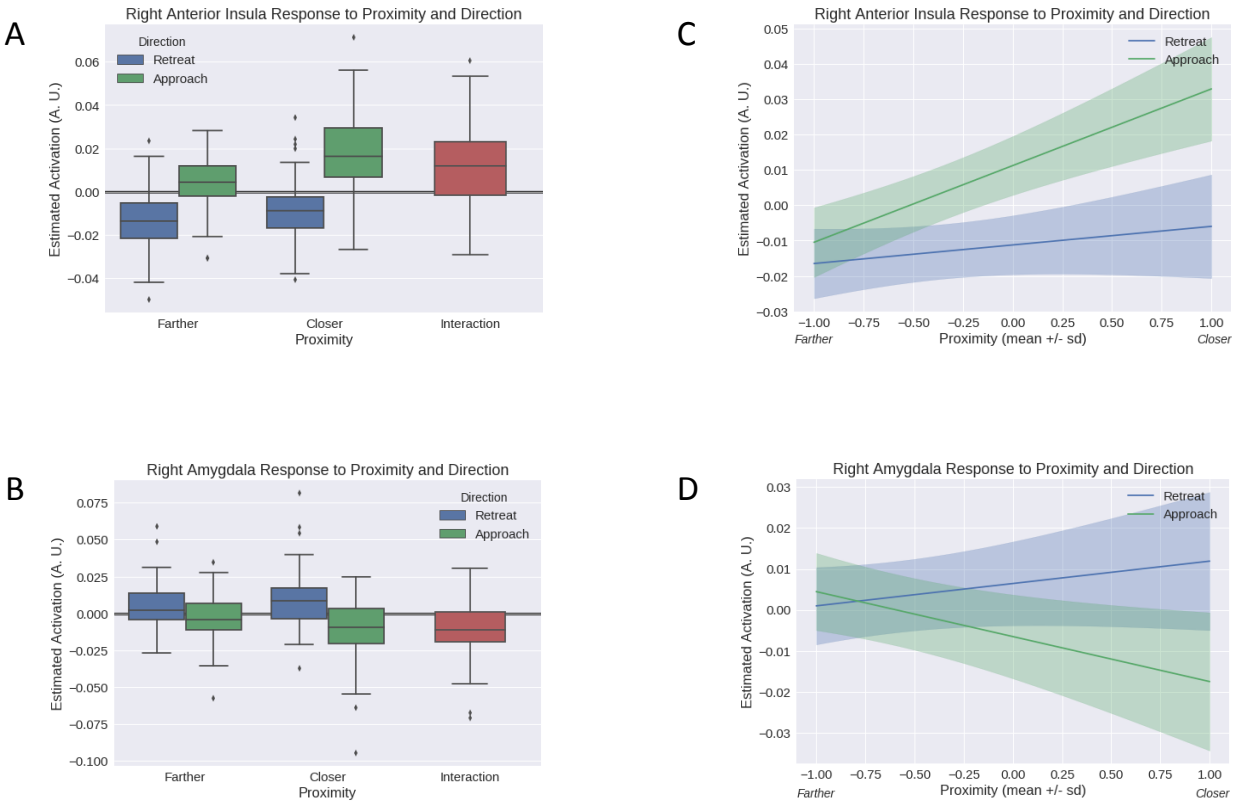
A
Right Anterior Insula Response to Proximity and Direction
Direction
Retreat
Approach
Estimated Activation (A. U.)
0.06
0.04
0.02
0.00
−0.02
−0.04
Farther
Closer
Interaction
Proximity
C
Right Anterior Insula Response to Proximity and Direction
Retreat
Approach
Estimated Activation (A. U.)
0.05
0.04
0.03
0.02
0.01
0.00
−0.01
−0.02
−0.03
−1.00
−0.75
−0.50
−0.25
0.00
0.25
0.50
0.75
1.00
Farther
Proximity (mean +/- sd)
Closer
B
Right Amygdala Response to Proximity and Direction
Direction
Retreat
Approach
Estimated Activation (A. U.)
0.075
0.050
0.025
0.000
−0.025
−0.050
−0.075
−0.100
Farther
Closer
Interaction
Proximity
D
Right Amygdala Response to Proximity and Direction
Retreat
Approach
Estimated Activation (A. U.)
0.03
0.02
0.01
0.00
−0.01
−0.02
−0.03
−1.00
−0.75
−0.50
−0.25
0.00
0.25
0.50
0.75
1.00
Farther
Proximity (mean +/- sd)
Closer

Figure 7

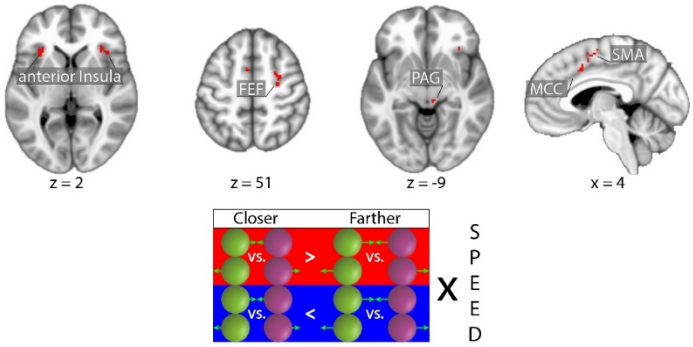
anterior Insula
z = 2
FEF
z = 51
PAG
z = -9
SMA
MCC
x = 4
Closer
Farther
vs.
>
vs.
vs.
<
vs.
X
SPEED

Figure 8

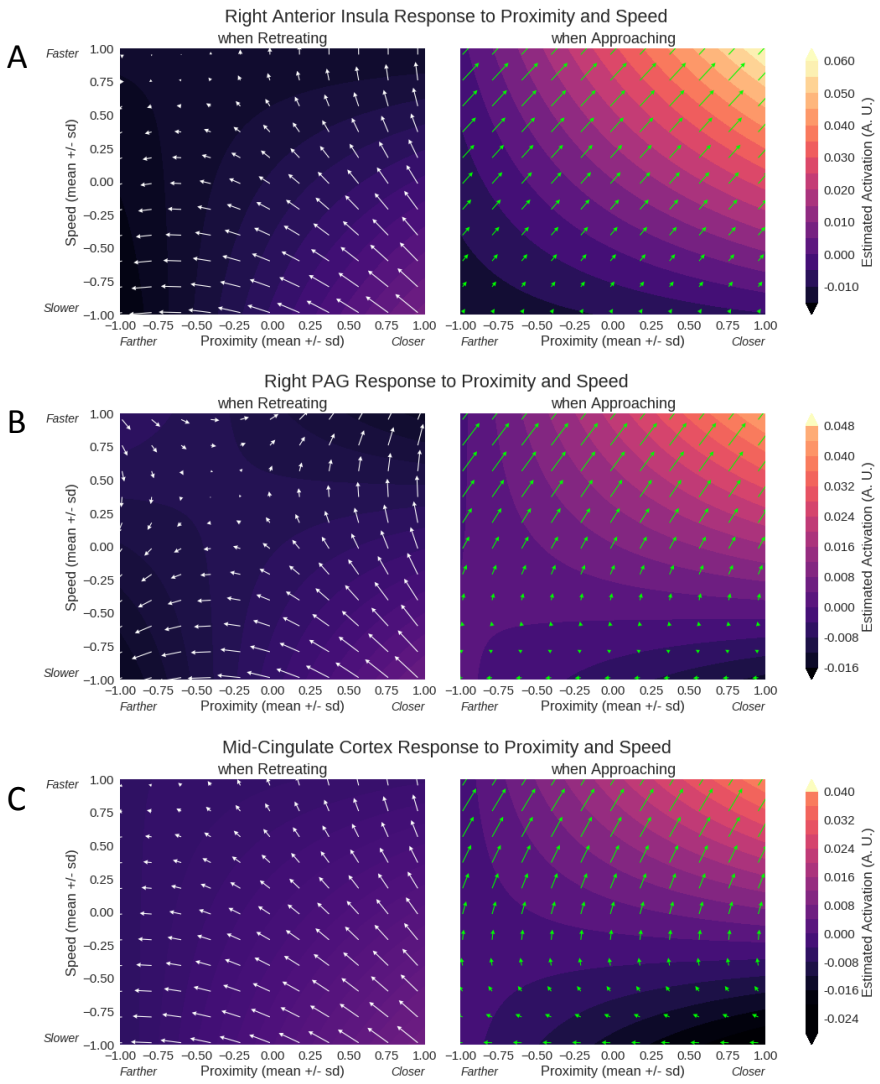
A
Right Anterior Insula Response to Proximity and Speed
when Retreating
when Approaching
Faster
Slower
Speed (mean +/- sd)
Farther
Proximity (mean +/- sd)
Closer
Estimated Activation (A. U.)
B
Right PAG Response to Proximity and Speed
C
Mid-Cingulate Cortex Response to Proximity and Speed

Figure 9

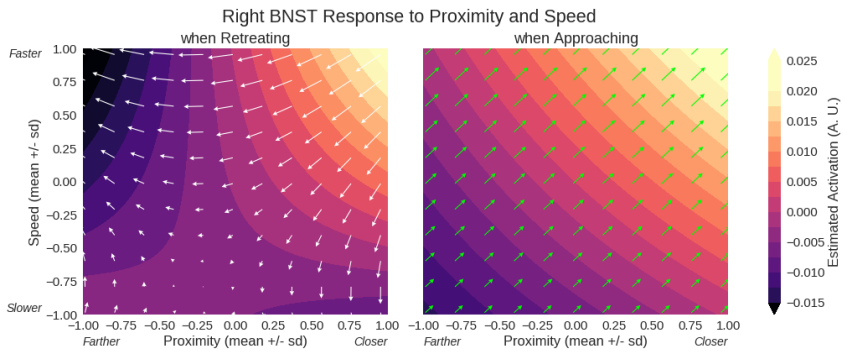
Right BNST Response to Proximity and Speed
when Retreating
when Approaching
Faster
Slower
Speed (mean +/- sd)
1.00
0.75
0.50
0.25
0.00
−0.25
−0.50
−0.75
−1.00
−1.00 −0.75 −0.50 −0.25 0.00 0.25 0.50 0.75 1.00
Farther
Proximity (mean +/- sd)
Closer
Estimated Activation (A. U.)
0.025
0.020
0.015
0.010
0.005
0.000
−0.005
−0.010
−0.015

Figure 10

A

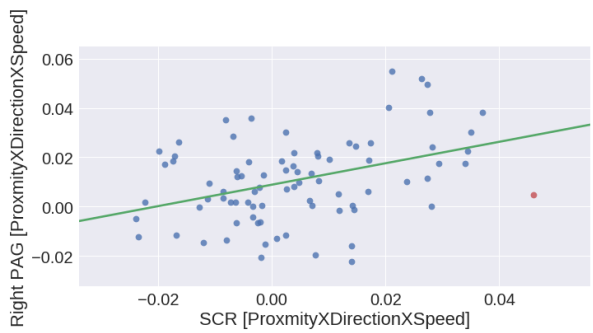
Right PAG [ProxmityXDirectionXSpeed]
0.06
0.04
0.02
0.00
−0.02
−0.02
0.00
0.02
0.04
SCR [ProxmityXDirectionXSpeed]

B

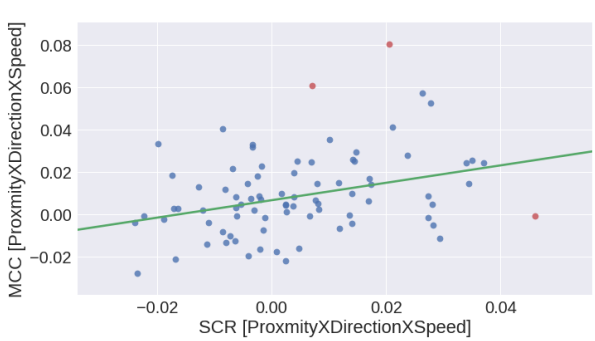
MCC [ProxmityXDirectionXSpeed]
0.08
0.06
0.04
0.02
0.00
−0.02
−0.02
0.00
0.02
0.04
SCR [ProxmityXDirectionXSpeed]

Figure 11